

See discussions, stats, and author profiles for this publication at: <https://www.researchgate.net/publication/231442092>

Experimental and ab initio studies of electronic structures of the trichloromethyl radical and cation

ARTICLE *in* JOURNAL OF THE AMERICAN CHEMICAL SOCIETY · JULY 1990

Impact Factor: 12.11 · DOI: 10.1021/ja00171a015

CITATIONS

40

READS

14

4 AUTHORS, INCLUDING:



Jeffrey W Hudgens

National Institute of Standards and Techn...

135 PUBLICATIONS 2,249 CITATIONS

SEE PROFILE



Russell Johnson

National Institute of Standards and Techn...

77 PUBLICATIONS 1,271 CITATIONS

SEE PROFILE

Experimental and ab Initio Studies of Electronic Structures of the CCl₃ Radical and Cation

Jeffrey W. Hudgens,^{*,†} Russell D. Johnson, III,^{*,†} Bilin P. Tsai,^{‡,§} and Sherif A. Kafafi^{*,‡}

Contribution from the Chemical Kinetics Division, Center for Chemical Technology, National Institute of Standards and Technology,[†] Gaithersburg, Maryland 20899, and Department of Environmental Chemistry and Biology, Johns Hopkins University School of Hygiene and Public Health, 615 North Wolfe Street, Baltimore, Maryland 21205. Received January 8, 1990

Abstract: The structures and optical spectroscopy of the CCl₃ radical and cation were studied by ab initio molecular orbital calculations and by experiment. The structures of the \tilde{X}^1A_1' (D_{3h}) state of the CCl₃ cation and the \tilde{X}^2A_1 (C_{3v}) and \tilde{X}^2A_2'' (D_{3h}) structures of the CCl₃ radical were optimized by ab initio calculations using the 6-31G* basis set. The optimized structure of the CCl₃ cation is a D_{3h} structure with $r_e(\text{C-Cl}) = 1.6437 \text{ \AA}$. The ground state of the CCl₃ radical is of \tilde{X}^2A_1 (C_{3v}) symmetry with $r_e(\text{C-Cl}) = 1.7142 \text{ \AA}$ and $\angle(\text{Cl-C-Cl}) = 117.10^\circ$. Vibrational frequencies for each CCl₃ species were computed. The electronic spectrum of C³⁵Cl₃ radicals was observed between 336 and 440 nm using mass resolved resonance enhanced multiphoton ionization (REMPI) spectroscopy. This spectrum arose from two-photon resonances with planar Rydberg states. A third laser photon ionized the radicals. One Rydberg series of quantum defect $\delta = 0.545$ is comprised of the \tilde{E}^2E' (3p) state ($\nu_{0-0} = 47170 \text{ cm}^{-1}$, $\omega_1(a_1' \text{ sym str}) = 544(6) \text{ cm}^{-1}$, $\omega_2'(a_2'' \text{ OPLA}) = 509(21) \text{ cm}^{-1}$, spin-orbit splitting = $33(5) \text{ cm}^{-1}$) and the \tilde{K}^2E' (4p) state ($\nu_{0-0} = 56236 \text{ cm}^{-1}$, $\omega_2' = 526(16) \text{ cm}^{-1}$). A second Rydberg series of $\delta = 0.50$ is comprised of the \tilde{F}^2A_2'' (3p) state ($\nu_{0-0} = 47868 \text{ cm}^{-1}$, $\omega_2' = 528(3) \text{ cm}^{-1}$) and the \tilde{L}^2A_2'' (4p) state ($\nu_{0-0} = 56409 \text{ cm}^{-1}$, $\omega_2' = 533(15) \text{ cm}^{-1}$). A third Rydberg series ($\delta = 0.216$) was comprised of the \tilde{G} (3d) ($\nu_{0-0} = 51218 \text{ cm}^{-1}$, $\omega_2' = 520(17) \text{ cm}^{-1}$) and \tilde{M} (4d) ($\nu_{0-0} = 57733 \text{ cm}^{-1}$, $\omega_2' = 542(3) \text{ cm}^{-1}$) states. A fit of the Rydberg formula to these series found the adiabatic ionization potential of the CCl₃ radical to be $IP_a = 8.109(5) \text{ eV}$. The \tilde{J}^2A_1' (4s) Rydberg state ($\nu_{0-0} = 53471 \text{ cm}^{-1}$, $\omega_2' = 530(20) \text{ cm}^{-1}$) was also observed. The REMPI spectrum exhibited the $\nu_2'' = 1-4$ vibrational hot bands of the \tilde{X}^2A_1 (C_{3v}) radical. Modeling of these hot bands derived the inversion barrier, $B_{\text{inv}} = 460 \pm 40 \text{ cm}^{-1}$.

I. Introduction

Gas-phase trichloromethyl (CCl₃) radicals appear in chemical processes of environmental and commercial importance. For example, the production of CCl₃ radicals from burning industrial waste can account for the CHCl₃ which evolves from incinerators.¹ In the upper atmosphere CCl₃ radicals formed by photolysis of freons eventually degrade to chlorine atoms that accelerate ozone depletion.² The manufacture of gallium arsenide (GaAs) microelectronic chips commonly uses RF discharges of CCl₄ gas to etch the semiconductor substrates.^{3,4} Since RF discharges of CCl₄ gas produce CCl₃ radicals,⁵ the CCl₃ radical may play an important role in the gas-surface chemistry. Thus, the importance of these processes justifies an increased effort to determine unknown physical properties of CCl₃ radicals and to measure new kinetic rates involving CCl₃ radicals.

In this paper we report our theoretical and experimental studies on the structure and spectroscopy of the CCl₃ radical and cation. In the theoretical section of this paper we provide the framework that supports discussions of structure and spectroscopy. We construct this framework by presenting qualitative molecular orbital theory (QMOT) descriptions and ab initio calculations for these species. These QMOT descriptions outline the principal interactions that cause the geometries and normal mode frequencies of CCl₃ radical and cation to differ. We present the results of ab initio calculations which quantitatively predict structures, vibrational frequencies, and relative energies of CCl₃ species.

In the Experimental Section we report the first vibrationally resolved electronic spectrum of the CCl₃ radical. The spectrum was observed between 336 and 440 nm by resonance enhanced multiphoton ionization (REMPI) spectroscopy. We have measured vibrational frequencies of modes associated with ground- and Rydberg-state CCl₃ radicals. For the ground-state CCl₃ radical our spectral analysis establishes the ionization potential, estimates the $\angle(\text{Cl-C-Cl})$ equilibrium apex angle, and determines the height of the barrier to inversion between the two structural

conformations. These experimentally derived values are compared with the ab initio results. Moreover, the REMPI scheme presented here is suitable for sensitive and selective detection of gas-phase CCl₃ radicals in other experiments.

Prior spectroscopic and structural information about the CCl₃ radical and cation is sparse. ESR spectroscopy has established that the ground state of CCl₃ radical is nonplanar.⁶ Only the infrared absorptions of the ν_3 degenerate stretch modes of the CCl₃ radical and cation are known.⁷ A broad ultraviolet absorption between 195 and 260 nm observed in the liquid⁸ and gas^{9,10} phases is attributed to CCl₃ radicals. Breitbarth and Berg¹¹ have proposed that the broad band emission observed between 420 and 700 nm from rf discharges of CCl₄ originates from electronically excited CCl₃ radicals.

Prior measurements establish that the ionization potential of the CCl₃ radical lies between 7.9 and 8.3 eV. Using electron impact ionization, Lossing¹² measured the CCl₃ ionization potential of $IP = 8.28 \text{ eV}$. Lias and Ausloos¹³ found limits for ΔH_f° (CCl₃⁺) by observing the ion-molecule reactions:



Combining these observations with the currently accepted heats

- (1) Oppelt, E. T. *Environ. Sci. Technol.* **1986**, *20*, 312.
- (2) *Chemical Kinetics of Small Radicals*; Alfassi, Z. B., Ed.; CRC Press: Boca Raton, FL, 1988; Vol. 3, p 41.
- (3) Smolinsky, G.; Gottscho, R. A.; Abys, S. M. *J. Appl. Phys.* **1983**, *54*, 3518.
- (4) Tokuda, J.; Takai, J.; Nakai, H.; Gamo, K.; Namba, S. *J. Opt. Soc. Am. B* **1987**, *4*, 267.
- (5) Breitbarth, F.-W.; Tiller, H.-J.; Reinhardt, R. *Plasma Chem. Plasma Process.* **1985**, *5*, 5717.
- (6) Hesse, C.; Leray, C.; Rocin, J. *Mol. Phys.* **1971**, *22*, 137.
- (7) Jacox, M. J. *Phys. Chem. Ref. Data* **1984**, *13*, 945.
- (8) Lesigne, B.; Gilles, L.; Woods, R. J. *Can. J. Chem.* **1974**, *52*, 1135.
- (9) Danis, F.; Caralp, F.; Veyret, B.; Loirat, H.; Lesclaux, R. *Int. J. Chem. Kinet.* **1989**, *21*, 715.
- (10) Russell, J. J.; Seetula, J. A.; Gutman, D.; Danis, F.; Caralp, F.; Lightfoot, P. D.; Lesclaux, R.; Melius, C. F.; Senkan, S. M. *J. Phys. Chem.* **1990**, *94*, 3277.
- (11) Breitbarth, F.-W.; Berg, D. *Chem. Phys. Lett.* **1988**, *149*, 334.
- (12) Lossing, F. P. *Bull. Soc. Chim. Belg.* **1972**, *81*, 125.
- (13) Lias, S. G.; Ausloos, P. *Int. J. Mass Spectrom. Ion Phys.* **1977**, *23*, 273.

* Address correspondence to these authors.

[†] National Institute of Standards and Technology.

[‡] On sabbatical leave from the University of Minnesota at Duluth.

[§] Johns Hopkins University School of Hygiene and Public Health.

[†] Formerly called the National Bureau of Standards.

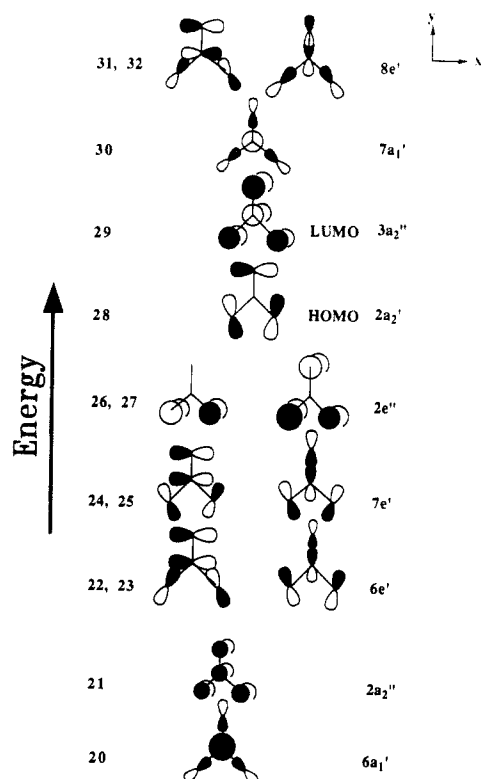


Figure 1. The highest occupied nine MO's and lowest empty four MO's of CCl_3^+ cation as obtained from ab initio HF/STO-3G calculations.

of formation¹⁴ for these reactants, we find $201.3 \leq \Delta H_f^\circ_{298}(\text{CCl}_3^+) \leq 207.2 \text{ kcal mol}^{-1}$. These values and $\Delta H_f^\circ_{298}(\text{CCl}_3) = 19.0 \text{ kcal mol}^{-1}$ ¹⁵ lead to the prediction that $\text{IP}_a = 7.90\text{--}8.16 \text{ eV}$.

II. Approximate Descriptions of the CCl_3 Cation and Radical

A purpose of molecular orbital theory is to quantitatively predict the structure and spectra of molecules. Explicit calculations of electronic spectra usually require the use of MRD CI or MCSCF computer codes which simultaneously compute a large set of excited electronic configurations. Such calculations require great effort and resources. At present chemical species with large numbers of electrons, such as the CCl_3 radical, are inaccessible to these codes.

Extensive calculations are not required to predict the vibrational structure observed in spectra which involve transitions between the ground state and a Rydberg state. In many cases ab initio calculations of the ground-state cation can predict the vibrational frequencies of the Rydberg radical to a good approximation. This approach can work because Rydberg radical wave functions are usually well described by:

$$\Psi = [\Phi_e \Phi_{\text{vib}} \Phi_{\text{rot}}]_{\text{cation}} \Phi_{\text{Ryd}}$$

where Φ_e , Φ_{vib} , and Φ_{rot} are the electronic, vibrational, and rotational wave functions of the cation, and Φ_{Ryd} is the hydrogenic Rydberg orbital wave function.^{16,17} The Rydberg electron resides in a hydrogenic s, p, d, ... orbital that lies mostly outside of the valence shells of the atoms in the radical. The electronic energies at which each Rydberg state resides may be estimated using the Rydberg formula. Because the Rydberg electron usually interacts weakly with the molecular core, the wave function that describes

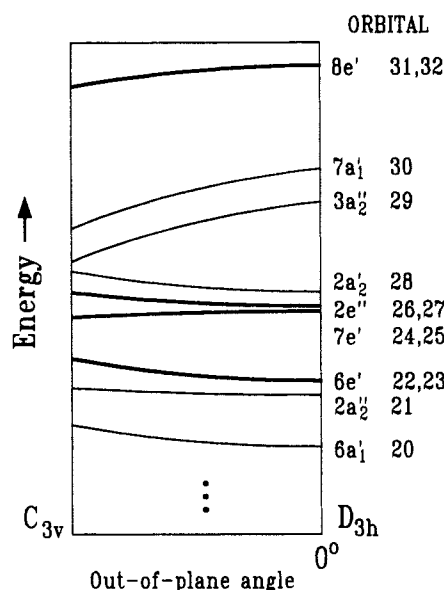


Figure 2. The Walsh diagram for AB_3 species which shows the change in energy of each molecular orbital as a function of out-of-plane angle, θ .

the bonding and mechanical motion of the molecular core is almost the same as in the cation. Thus, the geometry and vibrational spectra of Rydberg states should be nearly the same as those of the cation.

Below, we present the qualitative molecular orbital theory (QMOT) descriptions which outline the molecular orbital interactions of CCl_3 species. The QMOT descriptions predict the geometries and vibrational potential energy surfaces of the radicals and cation. These predictions will help us differentiate between Rydberg and valence upper state assignments for the REMPI spectra.

A. QMOT Description of the CCl_3 Cation. Figure 1 diagrams the 13 higher energy molecular orbitals (MO's 20–32) of CCl_3^+ which greatly influence molecular bonding and the overall geometry. These orbitals are constructed from the results of a HF/STO-3G calculation of CCl_3^+ constrained to D_{3h} symmetry. (The first 19 occupied orbitals, MO's 1–19, which lie at very low energies, are not shown.) MO's 20–28 are fully occupied. MO's 29–32 are unoccupied. As shown in Figure 1, there are four π -MO's: 21, 26, 27, and 29. π -MO 21 has C–Cl bonding interactions. The degenerate $2e''$ π -MO's 26 and 27 are nonbonding. The highest occupied MO (HOMO), MO 28, is chlorine–chlorine antibonding by through-space interactions and is carbon–chlorine π -nonbonding. π^* -MO 29, the lowest unoccupied MO (LUMO), is C–Cl antibonding. The remaining nine MO's are of the σ type. σ -MO's 20–25 have bonding interactions. The higher energy orbitals, σ^* -MO's 30–32, have antibonding interactions.

The energy ordering of the molecular orbitals depicted in Figure 1 agrees qualitatively with the diagram derived by Gimarc,¹⁸ who used extended Hückel calculations to model AB_3 molecules belonging to the D_{3h} point group. However, in disagreement with our ab initio calculation the extended Hückel calculations predict that the $7a_1'$ antibonding orbital (σ^* -MO 30) should lie higher in energy than the $8e'$ antibonding orbital (σ^* -MO's 31, 32). The extended Hückel calculations also predict that the $7e'$ orbitals (σ -MO's 24, 25) will lie higher than the $2e''$ π -nonbonding orbitals (MO's 26, 27). Previous studies have shown that the extended Hückel method tends to overestimate the energies of σ -MO's that engage in antibonding interactions.¹⁹ Therefore, the relative energies of the σ orbitals, $7e'$ and $7a_1'$, as predicted from extended Hückel calculations, are most likely too high. We believe that the MO ordering presented here is a more accurate description

(14) Lias, S. G.; Bartmess, J. E.; Holmes, J. L.; Levin, R. D.; Liebman, J. F.; Mallard, G. J. *Phys. Chem. Ref. Data* 1983, Suppl. Ser. No. 1.

(15) Mendenhall, G. D.; Golden, D. M.; Benson, S. W. *J. Phys. Chem.* 1973, 77 2702.

(16) *Advances in Multiphoton Processes and Spectroscopy*; Lin, S. H., Ed.; World Scientific Publishing Co.: Singapore, 1988, Vol. 4, pp 171–296.

(17) When using this wave function approximation, we must be aware of the potential complications that can invalidate its use. See, for example: *Chemical Spectroscopy and Photochemistry in the Vacuum-Ultraviolet*; Sandorfy, C., Ausloos, P. J., Robin, M. B., Eds.; D. Reidel: Boston, 1974; pp 113–127.

(18) Gimarc, B. M. *Molecular Structure and Bonding*; Academic Press: New York, 1979.

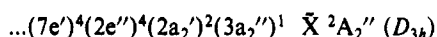
(19) Lowe, J. P. *Quantum Chemistry*; Academic Press: New York, 1978; pp 283–303.

of AB_3 species of the D_{3h} point group. Furthermore, this MO ordering based upon the STO-3G basis set is identical with the MO ordering calculated using the 6-31G* basis set.

QMOT analysis predicts that ground-state CCl_3^+ possesses a D_{3h} geometry and harmonic vibrational potentials along each normal mode. The prediction of a D_{3h} geometry is seen by examining the first-order energy changes of the occupied MO's as the planar D_{3h} CCl_3^+ is transformed to a C_{3v} geometry.²⁰ This $C_{3v} \leftarrow D_{3h}$ transformation is accomplished by a symmetric out-of-plane (OPLA) bending motion. Figure 2 presents the Walsh diagram for AB_3 species. This diagram shows the first-order energy changes of each molecular orbital as a function of out-of-plane angle, θ . (When $\theta = 0^\circ$, CCl_3 is planar.) The OPLA motion destabilize σ -MO 20 and π -MO 21 by reducing the C-Cl bonding interactions. The OPLA motion destabilizes the $6e'$ orbitals (σ -MO's 22, 23) by reducing the bonding overlap between the carbon and chlorine p-orbitals. The $2e''$ orbitals (π -MO's 26, 27) are also destabilized, but to a lesser degree, as the out-of-plane large amplitude (OPLA) motion moves the chlorine atoms together, which increases the repulsion between the out-of-phase chlorine p-orbitals. The bending motion also destabilizes π -MO 28 by increasing the through-space antibonding repulsions between the p-orbitals centered on the adjacent chlorine atoms. In contrast, the OPLA deformation stabilizes the $7e'$ orbitals (σ -MO's 24, 25) by decreasing the antibonding interaction between the carbon and chlorine p-orbitals. In summary, any OPLA motion of CCl_3^+ away from the D_{3h} geometry destabilizes (i.e., raises the energy of) four orbitals and stabilizes (i.e., lowers the energy of) two orbitals. The net energy minimum of the CCl_3^+ should lie at the planar D_{3h} structure. Because OPLA motion from the planar cation raises its total energy, the OPLA potential possesses a single minimum. We expect ν_2 OPLA vibrational energy levels to be evenly spaced and to fit a harmonic energy function.

Moreover, using arguments similar to those described above, additional analyses predict that any bond stretching or in-plane bending away from the D_{3h} geometry should also raise the total energy of CCl_3^+ . Therefore, the potential energy surface along each normal mode should possess a minimum centered at the D_{3h} structure. The vibrational spectra of all normal modes of CCl_3^+ should display evenly spaced energy levels characteristic of harmonic potentials.

B. The QMOT Description of the Ground-State CCl_3 Radical. Adding an electron to CCl_3^+ forms the CCl_3 radical. This radical electron will occupy π^* -MO 29 (Figure 1). If planar, the ground-state radical would have the configuration:

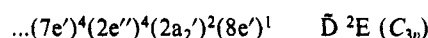
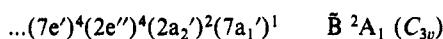
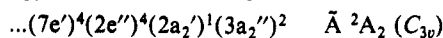


When the radical has a C_{3v} geometry, it is designated \tilde{X}^2A_1 .

As explained above, the net energy of fully occupied MO's 1-28 favors a planar structure. However, as the CCl_3 radical is transformed into a C_{3v} geometry, the singly occupied MO (SOMO), π^* -MO 29, becomes stabilized as it loses antibonding repulsion between the carbon and chlorine p_z-orbitals. Since π^* -MO 29 is a frontier orbital, the stabilization energy obtained with small OPLA motion should dominate over the energy contributions of all other MO's. However, as the OPLA bend becomes more acute, the energy changes of the destabilized MO's (MO's 20-23 and 26-28) should dominate over the stabilized MO's (MO's 24, 25, 29). The total energy as a function of the out-of-plane angle, θ , creates a double minimum potential energy function along the OPLA coordinate with minima that lie above (at $+\theta_m$) and below (at $-\theta_m$) the planar geometry. In the OPLA coordinate the inversion energy barrier, B_{inv} , is centered at the planar geometry. Therefore, the CCl_3 radical should possess a pyramidal geometry similar to ammonia. The ν_2'' OPLA vibrational energy levels should exhibit the irregular spacings induced

by the double-well potential function.

C. The QMOT Description of Electronically Excited CCl_3 Radicals. A QMOT analysis also predicts that the excited valence states of CCl_3 radical all possess pyramidal C_{3v} geometries. The lowest energy valence states will possess the configurations:



As described before for the \tilde{X}^2A_1 state, an OPLA excursion stabilizes the doubly occupied, frontier $3a_2''$ orbital (π^* -MO 29) through the loss of antibonding repulsions between the carbon and chlorine p_z-orbitals. In the \tilde{B}^2A_1 radical the OPLA excursion stabilizes σ^* -MO 30 frontier orbitals by reducing repulsions between the carbon s-orbital and chlorine p-orbitals. In the \tilde{D}^2E radical the OPLA excursion stabilizes σ^* -MO 31, 32 frontier orbitals by reducing repulsions between the carbon p-orbitals and chlorine p-orbitals. It is expected that the ν_2 OPLA vibrational energy levels of these excited valence states will exhibit the irregular spacings characteristic of double-well potential functions.

Because the CCl_3 radical possesses a C_{3v} structure, the energies of the higher valence states are difficult to calculate with our programs. To converge, our ab initio program requires the radical symmetry to be constrained to the C_{2v} point group. For the present work we can derive equally serviceable energy estimates by comparing the CCl_3 valence states to the analogous states that we have calculated for the CHCl_2 radical.²¹ In CCl_3 the \tilde{D}^2E state (which has one electron in MO 31, 32) has its analogue in the state of CHCl_2 which has the configuration $\dots(9a_1)^2(7b_2)^2(2a_2)^2(8b_2)^1$ (i.e., one electron in MO 23 of ref 21). This transition structure of the excited CHCl_2 radical lies at 44 114 cm^{-1} . By analogy, we estimate that the \tilde{D}^2E state of the CCl_3 radical should lie near 44 000 cm^{-1} .

By similar analysis we estimate that the \tilde{B}^2A_1 state of the CCl_3 radical should lie near 25 000 cm^{-1} . The configuration of the \tilde{B}^2A_1 CCl_3 radical which has one electron in MO 30 corresponds to the \tilde{B}^2A_1 state of the CHCl_2 radical which has one electron in the MO 22 of ref 21. Although we have no corresponding calculation for the CHCl_2 radical, we estimate that the \tilde{A}^2A_2 state of the CCl_3 radical should lie slightly below the \tilde{B}^2A_1 state.

III. Apparatus and Methods

A. Computational Methods. All ab initio molecular orbital (MO) calculations were performed with the GAUSSIAN 86 series of programs using the polarized 6-31G* basis set.²² The restricted Hartree-Fock (RHF) level of theory was applied to compute the equilibrium geometry of CCl_3^+ . The corresponding unrestricted treatment (UHF) was used to compute open shell CCl_3 radical species. Throughout these calculations all carbon-chlorine bond lengths were assumed equal. The use of Møller-Plesset (MP) perturbation theory to fourth order (MP4/6-31G*) partially accounted for the effects of electron correlation. These Møller-Plesset calculations are single point, frozen core (FC), MP4 calculations which used the optimum geometries obtained from the RHF and UHF/6-31G* treatments. All single, double, and quadruple excitations (MP4SDQ = FC/6-31G*) were included in these computations. Vibrational frequencies and zero-point energies (ZPE) were calculated at the RHF/6-31G* and UHF/6-31G* levels of theory for the CCl_3^+ and CCl_3 radicals, respectively.

All computations reported in this study were performed on an IBM 4381 computer at the Johns Hopkins University Academic Data Center Facility.

B. Experimental Apparatus. The apparatus and procedures used during this study are described in detail elsewhere.²³ Briefly, the apparatus consisted of a flow reactor which produced CCl_3 radicals, an excimer pumped dye laser which ionized the radicals, a time-of-flight mass spectrometer, and a computer/data acquisition system. Radicals

(21) Kafafi, S. A.; Hudgens, J. W. *J. Phys. Chem.* **1989**, *93*, 3474.

(22) Frisch, M. J.; Binkley, J. S.; Schlegel, H. B.; Raghavachari, K.; Melius, C. F.; Martin, R. L.; Stewart, J. J. P.; Bobrowicz, F. W.; Rohlfing, C. M.; Kahn, R. L.; Defrees, D. J.; Seeger, R.; Whiteside, R. A.; Fox, D. J.; Fleuder, E. M.; Pople, J. A. Carnegie-Mellon Quantum Chemistry Publishing Unit: Pittsburgh PA, 1984.

(23) Johnson, R. D., III; Tsai, B. P.; Hudgens, J. W. *J. Chem. Phys.* **1988**, *89*, 4558.

(20) The doubly degenerate MO's, 22-27, as drawn in Figure 1, are the proper zeroth-order wave functions for an OPLA perturbation. To first order, the OPLA should not lift the degeneracy of any MO's. See: Kafafi, S. A.; Lowe, J. P. From Atoms to Polymers: Isoelectronic Analogies. In *Molecular Structure and Energetics*; Liebman, J. F., Greenberg, A., Eds.; VCH Publishers: New York, 1989; Vol. 11, pp 279-305. Reference 19, pp 364-368.

Table I. Ab Initio Total Energies, Inversion Barriers, and Adiabatic Ionization Potentials of CCl₃ Species Computed at Several Levels of Theory

species	electronic state	level of theory	total energy (hartrees)	inversion barrier, B_{inv} (cm ⁻¹)	adiabatic ion. pot. (eV) ^a
CCl ₃ cation	$\tilde{X}^1A_1' (D_{3h})$	HF/6-31G*	-1415.945 761		
		MP2 = FC/6-31G*//HF/6-31G*	-1416.469 084		
		MP3 = FC/6-31G*//HF/6-31G*	-1416.495 629		
		MP4 = FC/6-31G*//HF/6-31G*	-1416.504 463		
CCl ₃ radical	$\tilde{X}^2A_1 (C_{3v})$	UHF/6-31G*	-1416.248 160	610	8.25
		UMP2 = FC/6-31G*//UHF/6-31G*	-1416.749 148	785	7.65
		UMP3 = FC/6-31G*//UHF/6-31G*	-1416.784 384	625	7.88
		UMP4 = FC/6-31G*//UHF/6-31G*	-1416.790 320	620	7.80
CCl ₃ radical transition structure	$\tilde{X}^2A_2'' (D_{3h})$	UHF/6-31G*	-1416.245 389		
		UMP2 = FC/6-31G*//UHF/6-31G*	-1416.745 571		
		UMP3 = FC/6-31G*//UHF/6-31G*	-1416.781 530		
		UMP4 = FC/6-31G*//UHF/6-31G*	-1416.787 500		

^a Derived using the UHF/6-31G* zero-point energies given in Table II.**Table II.** Physical Properties Obtained from HF/6-31G* (for CCl₃⁺) and UHF/6-31G* (for CCl₃ Radical Structures) ab Initio Calculations. Experimental Values Are Given in Parentheses

physical property	CCl ₃ cation	CCl ₃ radical	CCl ₃ radical transition structure
state designation	\tilde{X}^1A_1'	\tilde{X}^2A_1	\tilde{X}^2A_2''
point group	D_{3h}	C_{3v}	D_{3h}
$r_e(\text{C-Cl})$, Å	1.6437	1.7142	1.7022
$\angle(\text{Cl-C-Cl})$, deg	120.0	117.1 (116.7 ± 0.2) ^a	120.0
θ_m , deg	0.0	9.9 (10.6 ± 0.3) ^a	0.0
adiabatic IP, eV		8.25 (8.109 ± 0.005) ^a	
B_{inv} , cm ⁻¹		610 (460 ± 40) ^a	
ω_1 C-Cl ₃ sym str, cm ⁻¹	a_1' 521 ^b (544) ^c	a_1 487 ^b	a_1' 454
ω_2 OPLA bend, cm ⁻¹	a_2'' 514 ^b (509) ^c	a_1 322 ^{d,e} (251) ^{a,e}	a_2'' ^f
ω_3 deg str, cm ⁻¹	e' 1004 ^b (1037) ^g	e 901 ^b (898) ^g	e' 932
ω_4 deg def, cm ⁻¹	e' 302 ^b	e 266 ^b	e' 293
zero-point energy, cm ⁻¹	1824	1609 ^h	

^a An experimental result of this work. ^b Value is the ab initio frequency reduced by 11%. See text. ^c Based upon the experimental \tilde{E} Rydberg state frequency of this work. ^d Ab initio frequency derived from double minimum potential. See text. ^e $\nu_2'' = 0-2$ frequency interval. ^f Imaginary frequency indicative of transition structure. ^g Infrared Ar matrix data from ref 7. ^h For the ν_2 mode the ab initio ZPE = 197.8 cm⁻¹.

were produced in a flow reactor by hydrogen abstraction from CHCl₃ by fluorine and chlorine atoms. These atoms were produced by passing halogen gas through a microwave discharge. Free radicals produced in the flow reactor effused into the ion source of the time-of-flight mass spectrometer where they were ionized by a focused laser beam (energy = 10–20 mJ/pulse; bandwidth = 0.2 cm⁻¹ fwhm; focal length = 250 mm). The concentration of radicals in the ion source is estimated to be $\sim 10^{10}/\text{cm}^3$. The mass spectrometer resolved the ions and those of the appropriate mass were selected and averaged with a gated integrator. The spectra shown here are composites of spectra taken with the laser dyes (Exciton Chemical Co.)²⁴ DMQ (346–377 nm), QUI (368–405 nm), DPS (395–415), and Stilbene 420 (412–430 nm). The spectra are uncorrected for the variation of laser beam power over the range of each laser dye.

IV. Results and Analyses

A. Theoretical Results. Tables I and II present the results of the ab initio calculations for CCl₃ species. The optimized geometries of CCl₃⁺ and the CCl₃ radical are presented. Results are also shown for the planar, D_{3h} CCl₃ radical structure for which only $r_e(\text{C-Cl})$ was optimized. Table I lists the total energy for the CCl₃ species at each level of theory. The optimum geometries of both the CCl₃ radical and cation conform to the QMOT predictions. The CCl₃ cation possesses a planar D_{3h} structure, and the nonplanar C_{3v} CCl₃ radical is more stable than the planar D_{3h} structure.

Table II presents the properties of each CCl₃ species obtained from the ab initio calculations for structures optimized with HF/6-31G* (CCl₃⁺) and UHF/6-31G* (CCl₃ radicals) levels of theory. In parentheses, Table II lists the experimentally derived value of each property. The presence of an imaginary ν_2 frequency

in the vibrational spectrum of the planar CCl₃ radical indicates that the planar structure is unstable and lies at the saddle point of the OPLA potential surface. Hence, we have labeled the planar radical as a transition structure. Because the GAUSSIAN 86 program consistently predicts harmonic vibrational frequencies that are 9–12% higher than the experimentally measured frequencies,²⁵ we have reduced the harmonic vibrational frequencies reported by this program by 11%. This scaling factor was not applied to the ν_2 OPLA frequency of the \tilde{X}^2A_1 radical presented in Table II.

Because the CCl₃ radical is pyramidal, the ν_2 OPLA mode of the radical is not harmonic. Instead, the OPLA potential possesses two potential energy minima. The ν_2'' OPLA vibrational frequency was calculated from the ab initio results by solving the Hamiltonian for a quartic oscillator with the double-well potential, $V = A(Z^4 - BZ^2)$, after the method described by Laane.²⁶ The OPLA coordinate is $Z = c_\mu r_e \theta$. The constant c_μ includes the reduced mass, r_e is the C–Cl bond length, and θ is the out-of-plane angle.²⁷ The reduced mass of the oscillator was approximated by the G -matrix element, $g_2 = (3m_{\text{Cl}} + m_{\text{C}})/3m_{\text{C}}m_{\text{Cl}}$. The mass-weighted coefficients, A and B , were derived from the variables (1) θ_m , the bending angle which corresponds to the minimum in the potential, (2) r_e , the C–Cl bond length, and (3) B_{inv} , the inversion barrier. We derived $B_{inv} = 610 \text{ cm}^{-1}$ from the difference between the ab initio energies of the CCl₃ radical and the CCl₃ radical transition structures (Table I). In Table II we present the $\nu_2 = 0-2$ interval derived from the ab initio structure. This interval would appear in an infrared absorption spectrum.

According to these quartic potential calculations, the nearly degenerate $\nu_2 = 0, 1$ levels lie only 1.1 cm⁻¹ apart. This near-

(24) Certain commercial materials and equipment are identified in this paper in order to adequately specify the experimental procedure. In no case does such an identification imply recommendation or endorsement by the National Institute of Standards and Technology, nor does it imply that the material or equipment identified is necessarily the best available for the purpose.

(25) Hehre, W. J.; Radom, L.; Schleyer, P. R.; Pople, J. *Ab Initio Molecular Orbital Theory*; Wiley-Interscience: New York, 1985.

(26) Laane, J. *Appl. Spectrosc.* 1970, 24, 73.

(27) The internal angle $\angle\text{Cl-C-Cl}$, is related to θ by the equation, $\angle(\text{Cl-C-Cl}) = 2 \sin^{-1} [(3/4)^{1/2} \cos \theta]$.

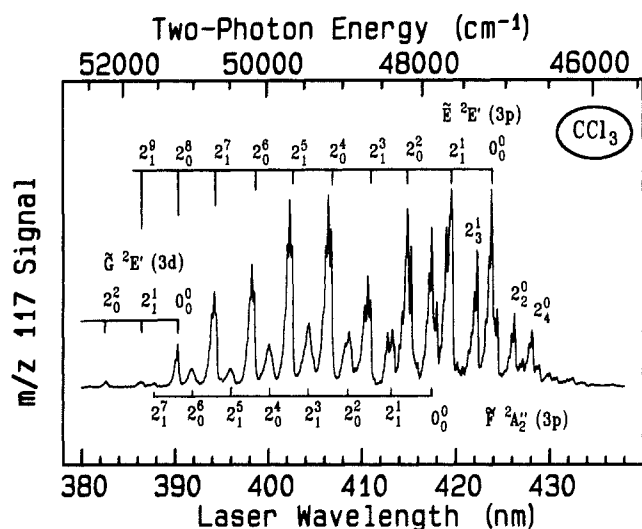
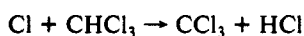
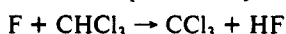


Figure 3. The composite REMPI spectrum of the $^{12}\text{C}^{35}\text{Cl}_3$ radical (m/z 117) observed between 380 and 440 nm.

degeneracy will cause the $v_2 = 0, 1$ levels to possess almost identical populations at ambient temperature. Thus, vibrational bands observed in electronic spectra originating from these levels should exhibit similar intensities.

Table I shows the adiabatic ionization potentials of CCl_3 radical computed at several levels of theory. We have derived the ab initio IP_a from the difference between the total electronic energies and the scaled zero-point vibrational energies of the CCl_3 cation and radical. At the UHF/6-31G* level of theory these calculations give $\text{IP}_a = 8.25$ eV, with an uncertainty of ± 0.2 eV.²⁷ Table I also shows values of IP_a derived from single-point calculations at higher levels of theory. Because these single-point calculations evaluate the total energy using the geometry optimized at the UHF/6-31G* level, the geometry changes induced by electron correlation are not found. Thus, the IP_a 's predicted by these single-point calculations are unreliable.

B. Radical Generation and Species Characterization. Figures 3 and 4 display the composite mass resolved REMPI spectra of the $^{12}\text{C}^{35}\text{Cl}_3$ radical (m/z 117) observed between 336 and 440 nm. The CCl_3 radicals were produced by the reactions:



Identical m/z 117 spectra were obtained from the flow reactor effluent of both reactions. Very similar m/z 119, 121, 123 REMPI spectra corresponding to $^{12}\text{C}^{35}\text{Cl}_{3-n}^{37}\text{Cl}_n$ ($n = 1, 2, 3$) radicals were also observed. The m/z 117, 119, 121, 123 ion signals were proportional to the reactant concentrations. Whenever the microwave discharge that generated the fluorine or chlorine atoms was extinguished, the REMPI signals ceased. Laser ionization did not appear to induce fragmentation and the REMPI spectra were carried only by molecular cations. Thus, all chemical and mass spectral data support the assignment of the REMPI spectrum to the CCl_3 radical.

C. The REMPI Spectrum of CCl_3 between 380 and 440 nm. Table III presents the band maxima observed in the REMPI spectrum of the $^{12}\text{C}^{35}\text{Cl}_3$ radical between 380 and 440 nm. As indicated by the state energies listed in Table III, we have assigned the spectrum to two-photon preparation of excited states (vide infra). In this paper we use the vibrational analysis of each electronic state to establish the photon order of each band system. This approach works reliably because the laser frequency intervals observed between spectral bands are submultiples of the actual vibrational frequencies of each electronic state. Our analysis will account for 83% of all observed vibrational bands and yield sensible vibrational frequencies and state assignments which also agree with the predictions of ab initio calculations. No sensible analyses of the REMPI spectra are possible using photon orders other than 2.

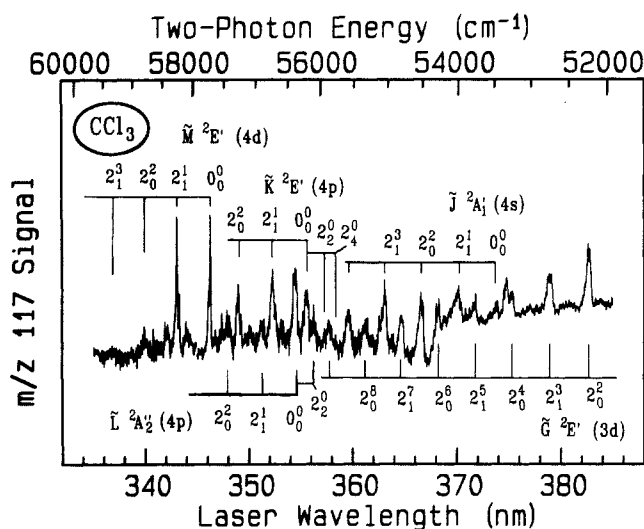


Figure 4. The composite REMPI spectrum of the $^{12}\text{C}^{35}\text{Cl}_3$ radical (m/z 117) observed between 334 and 386 nm.

The spectrum between 380 and 440 nm originates from two excited electronic states labeled as $\tilde{\text{E}}$ and $\tilde{\text{F}}$. Casual inspection shows that the $\tilde{\text{E}}$ and $\tilde{\text{F}}$ states are distinctly different. In Figure 3 the $\tilde{\text{E}}$ state bands appear as sharp doublets. Each doublet is separated by $33(5) \text{ cm}^{-1}$. The most intense progression of the $\tilde{\text{E}}$ state is comprised of nine members separated by $2\nu = 509(21) \text{ cm}^{-1}$. In contrast, the $\tilde{\text{F}}$ state bands appear as less intense, broader bands. The $\tilde{\text{F}}$ state bands lie interleaved between the $\tilde{\text{E}}$ state bands and exhibit an average band interval of $2\nu = 528(3) \text{ cm}^{-1}$. The $\tilde{\text{F}}$ state exhibits no conspicuous hot bands or combination bands which would help confirm the assignment of the electronic origin. Preliminary analysis could not resolve between an assignment of the $\tilde{\text{F}}$ state origin to the 413.22-nm band or to the 417.70-nm band.

We assign the most prominent vibrational progression of the $\tilde{\text{E}}$ and $\tilde{\text{F}}$ states to the ν_2' OPLA vibration (selection rule:²⁸ $\Delta\nu_2 = 0, \pm 2, \pm 4, \dots$). Each prominent ν_2' OPLA progression reflects the distinct change in equilibrium angle between the ground and upper electronic states. Analysis of the ν_2' OPLA mode intervals in each upper electronic state can distinguish between Rydberg and excited valence state assignments. The QMOT analysis predicts that each CCl_3 Rydberg state is planar and should possess a nearly harmonic potential energy function along its ν_2' coordinate. Therefore, we expect the cation to exhibit evenly spaced ν_2' energy levels. In contrast, the QMOT analysis predicts that excited valence states (cf. the $\tilde{\text{D}}^2\text{E}$ state) are pyramidal and should possess irregularly spaced manifolds of ν_2' energy levels. Because we observe regularly spaced ν_2' OPLA frequency intervals, we deduce that the $\tilde{\text{E}}$ and $\tilde{\text{F}}$ states are planar Rydberg states.

Attributing the spectra to Rydberg states clarifies the photoabsorption process that produces the ion signals. The adiabatic ionization potential of $\text{IP}_a = 7.9\text{--}8.3$ eV found by our ab initio calculations and estimated from the heats of formation of the radical and cation indicates that a CCl_3 radical may ionize after absorbing three laser photons. Because the Rydberg formula predicts that all Rydberg states of the CCl_3 radical reside at energies greater than 35000 cm^{-1} , these Rydberg states must lie at the energy of two laser photons. Thus, a CCl_3 Rydberg radical is formed by adsorbing two laser photons. After this Rydberg radical absorbs a third laser photon, it ionizes by ejecting the Rydberg electron to form the $\tilde{\text{X}}^1\text{A}'_1$ cation; i.e., the ion signals are generated through a $2 + 1$ REMPI mechanism.

Even if the analysis above is disregarded, we note that alternate assignments of the $\tilde{\text{E}}$ and $\tilde{\text{F}}$ band systems to one photon resonances with the $\tilde{\text{A}}^2\text{A}_2$ and $\tilde{\text{B}}^2\text{A}_1$ states conflict with the data. First, the $\tilde{\text{A}}^2\text{A}_2 \leftarrow \tilde{\text{X}}^2\text{A}_1$ transition is one-photon forbidden. Second, even

(28) A discussion of the vibrational selection rules that apply to the analysis of electronic spectra between pairs of $\text{C}_{3v}\text{--C}_{3v}$ and $\text{C}_{3v}\text{--D}_{3h}$ states is found in Johnson, R. D., III; Tsai, B. P.; Hudgens, J. W. *J. Chem. Phys.* **1989**, *91*, 3340.

Table III. Band Maxima Observed in the 2 + 1 *m/z* 117 REMPI Spectrum of the $^{12}\text{C}^{35}\text{Cl}_3$ Radical between 382 and 440 nm and Their Assignments³⁰

assignment	band maximum λ_{air} (nm)	two-photon energy (cm ⁻¹)	energy rel to $\tilde{\text{E}}^2\text{E}_a'$ (3p) origin (cm ⁻¹)	energy rel to $\tilde{\text{F}}^2\text{A}_2''$ (3p) origin (cm ⁻¹)	$\tilde{\text{F}}^2\text{A}_2''$ (3p) ν_2' interval (cm ⁻¹)
	430.81	46 411	-759		
	430.46	46 448	-722		
	430.00	46 499	-671		
	429.65	46 536	-634		
	428.93	46 614	-556		
	428.63	46 647	-523		
$\tilde{\text{E}}^2\text{E}_a' 2_0^0$	428.19	46 695	-475		
$\tilde{\text{E}}^2\text{E}_b' 2_0^0$	427.89	46 728	-442		
	427.17	46 807	-363		
	426.89	46 838	-332		
$\tilde{\text{E}}^2\text{E}_a' 2_2^0$	426.32	46 900	-270		
$\tilde{\text{E}}^2\text{E}_b' 2_2^0$	426.03	46 932	-238		
	424.98	47 048	-122		
	424.46	47 104	-66		
	424.16	47 134	-36		
$\tilde{\text{E}}^2\text{E}_a' (3p) 0_0^0$	423.88	47 170	0		
$\tilde{\text{E}}^2\text{E}_b' (3p) 0_0^0$	423.57	47 204	34		
$\tilde{\text{E}}^2\text{E}_a' 1_0^0 2_4^0$	423.25	47 240	70		
$\tilde{\text{E}}^2\text{E}_b' 1_0^0 2_4^0$	422.97	47 271	101		
$\tilde{\text{E}}^2\text{E}_a' 2_1^1$	422.29	47 347	177		
$\tilde{\text{E}}^2\text{E}_b' 2_1^1$	422.01	47 379	209		
$\tilde{\text{E}}^2\text{E}_a' 1_0^0 2_2^0$	421.40	47 447	277		
$\tilde{\text{E}}^2\text{E}_b' 1_0^0 2_2^0$	421.13	47 478	308		
$\tilde{\text{E}}^2\text{E}_a' 2_1^1$	419.59	47 652	482		
$\tilde{\text{E}}^2\text{E}_a' 2_2^1$	419.39	47 675	505		
$\tilde{\text{E}}^2\text{E}_b' 2_1^1$	419.29	47 686	516		
$\tilde{\text{E}}^2\text{E}_a' 1_0^0$	418.99	47 720	550		
$\tilde{\text{E}}^2\text{E}_b' 1_0^0$	418.72	47 751	581		
	418.02	47 832			
	417.70	47 868			
$\tilde{\text{F}}^2\text{A}_2'' (3p) 0_0^0$				0	
$\tilde{\text{E}}^2\text{E}_a' 1_0^0 2_1^1; \tilde{\text{E}}^2\text{E}_a' 2_2^1$	417.43	47 899	729		
$\tilde{\text{E}}^2\text{E}_b' 1_0^0 2_1^1; \tilde{\text{E}}^2\text{E}_b' 2_2^1$	417.18	47 928	758		
	415.59	48 111	941		
	415.31	48 143	973		
$\tilde{\text{E}}^2\text{E}_a' 2_2^0$	414.91	48 190	1020		519
$\tilde{\text{E}}^2\text{E}_b' 2_2^0$	414.86	48 196	1026		
$\tilde{\text{E}}^2\text{E}_a' 1_0^0 2_1^1$	414.63	48 222	1052		
$\tilde{\text{E}}^2\text{E}_b' 1_0^0 2_1^1$	414.25	48 267	1097		
$\tilde{\text{E}}^2\text{E}_a' 1_0^0$	413.97	48 300	1130		
$\tilde{\text{E}}^2\text{E}_a' 2_3^1$	413.49	48 356	1186		
$\tilde{\text{E}}^2\text{E}_b' 2_3^1; \tilde{\text{F}}^2\text{A}_2'' 2_1^1$	413.22	48 387	1217	519	
$\tilde{\text{E}}^2\text{E}_a' 1_0^0 2_2^1$	412.72	48 445	1275		
$\tilde{\text{E}}^2\text{E}_b' 1_0^0 2_2^1$	412.48	48 474	1304		
$\tilde{\text{E}}^2\text{E}_a' 2_1^1$	410.96	48 653	1483		
$\tilde{\text{E}}^2\text{E}_b' 2_1^1; \tilde{\text{E}}^2\text{E}_a' 1_0^0 2_2^0$	410.65	48 690	1520		526
$\tilde{\text{E}}^2\text{E}_b' 1_0^0 2_2^0$	410.35	48 725	1555		
$\tilde{\text{E}}^2\text{E}_a' 2_2^1; \tilde{\text{E}}^2\text{E}_a' 1_0^0 2_3^1; \tilde{\text{F}}^2\text{A}_2'' 2_0^0$	408.78	48 913	1743	1045	
$\tilde{\text{E}}^2\text{E}_b' 2_2^1; \tilde{\text{E}}^2\text{E}_b' 1_0^0 2_3^1$	408.62	48 931	1761		
$\tilde{\text{E}}^2\text{E}_a' 2_0^0$	406.72	49 160	1990		
$\tilde{\text{E}}^2\text{E}_b' 2_0^0; \tilde{\text{E}}^2\text{E}_a' 1_0^0 2_3^1$	406.41	49 197	2027		
$\tilde{\text{E}}^2\text{E}_b' 1_0^0 2_3^1; \tilde{\text{E}}^2\text{E}_a' 1_0^0 2_0^0$	406.11	49 234	2064		
$\tilde{\text{E}}^2\text{E}_b' 1_0^0 2_0^0$	405.84	49 266	2096		534
$\tilde{\text{E}}^2\text{E}_a' 2_3^1$	404.81	49 392	2222		
$\tilde{\text{F}}^2\text{A}_2'' 2_1^1$	404.36	49 447		1579	
$\tilde{\text{E}}^2\text{E}_a' 2_1^1$	402.55	49 669	2499		
$\tilde{\text{E}}^2\text{E}_a' 1_0^0 2_0^0; \tilde{\text{E}}^2\text{E}_b' 2_1^1$	402.28	49 703	2533		
$\tilde{\text{E}}^2\text{E}_a' 1_0^0 2_3^1; \tilde{\text{E}}^2\text{E}_b' 1_0^0 2_0^0$	401.99	49 738	2568		528
$\tilde{\text{E}}^2\text{E}_b' 1_0^0 2_3^1$	401.73	49 770	2600		
$\tilde{\text{E}}^2\text{E}_a' 2_2^1$	400.41	49 935	2765		
$\tilde{\text{F}}^2\text{A}_2'' 2_0^0$	400.09	49 975		2107	
$\tilde{\text{E}}^2\text{E}_a' 2_0^0$	398.49	50 176	3006		
$\tilde{\text{E}}^2\text{E}_b' 2_0^0; \tilde{\text{E}}^2\text{E}_a' 1_0^0 2_1^1$	398.21	50 211	3041		
$\tilde{\text{E}}^2\text{E}_b' 1_0^0 2_1^1; \tilde{\text{E}}^2\text{E}_a' 1_0^0 2_0^0$	397.95	50 244	3074		528
$\tilde{\text{E}}^2\text{E}_b' 1_0^0 2_0^0$	397.70	50 275	3105		

Table III (Continued)

assignment	band maximum λ_{air} (nm)	two-photon energy (cm ⁻¹)	energy rel to \tilde{E}^2E_a' (3p) origin (cm ⁻¹)	energy rel to \tilde{F}^2A_2'' (3p) origin (cm ⁻¹)	\tilde{F}^2A_2'' (3p) ν_2' interval (cm ⁻¹)
$\tilde{E}^2E_a' 2_3^7$	396.66	50 407	3237	2635	525
$\tilde{F}^2A_2'' 2_1^7$	395.91	50 503			
$\tilde{E}^2E_a' 2_1^7$	394.44	50 690	3420		
$\tilde{E}^2E_a' 1_0^6, \tilde{E}^2E_b' 2_1^7$	394.25	50 715	3545		
$\tilde{E}^2E_a' 1_0^6, \tilde{E}^2E_b' 1_0^6$	394.05	50 740	3570	3160	529
$\tilde{F}^2A_2'' 2_0^6$	391.83	51 028			
$\tilde{E}^2E_a' 2_0^6, \tilde{G}^2E' 0_0^6$	390.38	51 218	4048		
$\tilde{E}^2E_b' 2_0^6$	390.17	51 246	4076		
	389.72	51 305	4135	3689	
$\tilde{F}^2A_2'' 2_1^7$	387.81	51 557			
$\tilde{E}^2E_a' 2_1^7, \tilde{G}^2E' 2_1^7$	386.40	51 745	4575		
$\tilde{E}^2E_b' 2_1^7$	386.12	51 783	4613		

Table IV. The Deslandres Table Which Analyzes the ν_2 OPLA Mode Bands Observed in the \tilde{E}^2E_a' (3p) $\leftarrow \tilde{X}^2A_1$ REMPI Spectrum of the ¹²C³⁵Cl₃ Radical^a

ν' Even						
	$\nu'' = 0$		$\nu'' = 2$		$\nu'' = 4$	measured \tilde{E}^2E' (3p) ν_2' interval
$\nu' = 0$	47 170 973	270	46 900 999	205	46 695 980	984 (14) 2-0
$\nu' = 2$	48 143 1 016	244	47 899 1 014	224	47 675	1015 (1) 4-2
$\nu' = 4$	49 160 1 016	247	48 913 ^b 1 022			1019 (4) 6-4
$\nu' = 6$	50 176 1 042	241	49 935 ^b			1042 8-6
$\nu' = 8$	51 218					
av ω_2''		251 (14)		215 (13)		
measured $\tilde{X}^2A_1 \nu_2''$ interval		2-0		4-2		
ν' Odd						
	$\nu'' = 1$		$\nu'' = 3$		av ω_2'	measured \tilde{E}^2E' (3p) ν_2' interval
$\nu' = 1$	47 652 1 000	304	47 348 1 007		1004 (4)	3-1
$\nu' = 3$	48 653 1 016	297	48 356 1 036		1026 (10)	5-3
$\nu' = 5$	49 669 1 021	277	49 392 1 015		1018 (4)	7-5
$\nu' = 7$	50 690 1 056	283	50 407		1056	9-7
$\nu' = 9$	51 745					
av ω_2''		290 (12)				
measured $\tilde{X}^2A_1 \nu_2''$ interval		3-1				
av $\omega_2'/2 = 507$ (10) cm ⁻¹						

^a Energies and differences are in cm⁻¹. ^b Blended band.

though the $\tilde{B}^2A_1 \leftarrow \tilde{X}^2A_1$ transition is one-photon allowed, the electron configuration of CCl₃ (\tilde{B}^2A_1) radicals should enable optical ionization to prepare only electronically excited-state cations. This ionization step will require three or four laser photons. We expect this 1 + 3 (or 4) REMPI process to possess a much lower ionization cross section than a 2 + 1 REMPI process. Thus, alternate assignments of these spectra to one-photon resonances cannot explain the number of electronic states observed, their signal strength, or their vibrational structure.

Further vibrational analysis of the sharp doublet bands gives the \tilde{E} state electronic origin and the ν_2'' vibrational structure in the \tilde{X}^2A_1 state. Many weaker bands and shoulders observed throughout the $\tilde{E} \leftarrow \tilde{X}^2A_1$ REMPI spectrum arise from thermally populated ν_2'' vibrational levels of the ground state, i.e., ν_2'' hot bands. Table IV shows the Deslandres table which dissects the REMPI bands to show ω_2 vibrational intervals in the \tilde{E} state

and ground state. Consistent with the QMOT prediction, the ground-state vibrational intervals between $\nu_2'' = 0-4$ are irregular. The irregular ω_2'' intervals are symptomatic of the double-well potential surface along the ν_2'' OPLA coordinate. The analysis displayed in Table IV establishes that the lower energy doublet of the \tilde{F} state at 423.88 nm ($2h\nu = 47 170$ cm⁻¹) is an origin.

The ν_1' symmetric stretch mode (selection rule:²⁸ $\Delta\nu_1 = 0, \pm 1, \pm 2, \dots$) of the \tilde{E} Rydberg state contributes bands to the REMPI spectrum. The assignment of these bands confirms the assignment of the \tilde{E} state origin. Between 390 and 361 nm the REMPI spectrum displays progressions of bands that we have assigned to combinations involving ν_1' and ν_2' (Table III). The $\tilde{E} 1_0^1$ bands appear at 418.99 and 418.72 nm (Figure 3). The average of 19 combination differences between pairs of 2_1^7 and 1_0^6 bands gives the ν_1' CCl₃ symmetric stretch frequency, $\omega_1' = 544$ (6) cm⁻¹. The $\tilde{E} 1_0^1$ bands appear at 414.25 and 413.97 nm (Figure 3). The

Table V. Band Maxima Observed in the 2 + 1 *m/z* 117 REMPI Spectrum of the ¹²C³⁵Cl₃ Radical between 340 and 382 nm and Their Assignments

assignment	band maximum λ_{air} (nm)	two-photon energy (cm ⁻¹)	energy rel to nd origin (cm ⁻¹)	energy rel to \tilde{J}^2A_1' (4s) origin (cm ⁻¹)	energy rel to \tilde{K}^2E' (4p) origin (cm ⁻¹)	energy rel to \tilde{L}^2A_2'' (4p) origin (cm ⁻¹)
$\tilde{E}^2E'_2 2_0^0; \tilde{G}^2E'_2 0_0^0$	390.38	51 218	0			
$\tilde{E}^2E'_2 2_1^0; \tilde{G}^2E'_2 2_1^0$	386.40	51 733	515			
$\tilde{G}^2E'_2 2_0^0$	382.64	52 253	1035			
$\tilde{G}^2E'_2 2_1^0$	378.87	52 773	1555			
$\tilde{G}^2E'_2 2_0^0$	375.35	53 267	2049			
	374.85	53 339				
$\tilde{J}^2A_1' (4s) 0_0^0$	373.93	53 471		0		
$\tilde{G}^2E'_2 2_1^0$	371.84	53 771	2553			
$\tilde{J}^2A_1' 2_1^0$	370.23	54 005		534		
$\tilde{G}^2E'_2 2_0^0$	368.30	54 288	3070			
$\tilde{J}^2A_1' 2_0^0$	366.78	54 513		1042		
$\tilde{G}^2E'_2 2_1^0$	364.66	54 829	3611			
$\tilde{J}^2A_1' 2_1^0$	363.13	55 061		1590		
$\tilde{G}^2E'_2 2_0^0$	361.26	55 345	4127			
	359.61	55 600				
$\tilde{K}^2E'_2 2_0^0$	358.42	55 784			-452	
$\tilde{K}^2E'_2 2_1^0$	357.31	55 958			-278	
$\tilde{G}^2E'_2 2_1^0$	357.75	55 890	4672			
$\tilde{L}^2A_2'' 2_0^0$	356.27	56 122				-287
$\tilde{K}^2E'_2 (4p) 0_0^0$	355.54	56 236			0	
$\tilde{L}^2A_2'' (4p) 0_0^0$	354.46	56 409				0
	353.14	56 618				
$\tilde{K}^2E'_2 2_1^0$	352.32	56 751			515	
$\tilde{L}^2A_2'' 2_1^0$	351.23	56 927				518
$\tilde{K}^2E'_2 2_0^0$	349.01	57 288			1052	
$\tilde{L}^2A_2'' 2_0^0$	347.88	57 474				1065
$\tilde{M}^2E'_2 (4d) 0_0^0$	346.32	57 733	0			
$\tilde{M}^2E'_2 2_1^0$	343.11	58 274	541			
$\tilde{M}^2E'_2 2_0^0$	339.96	58 814	1081			
$\tilde{M}^2E'_2 2_1^0$	336.84	59 359	1626			

average of nine combination differences between pairs of 2_k^m and $1_0^m 2_k^m$ bands gives the $\nu_1' = 0-2$ interval, $2\omega_1' = 1084$ (9) cm⁻¹.

D. The REMPI Spectrum of CCl₃ between 334 and 386 nm. Between 386 and 334 nm the REMPI spectrum (Figure 4) of the ³⁵CCl₃ radical shows five vibrational progressions, labeled \tilde{G} , \tilde{J} , \tilde{K} , \tilde{L} , and \tilde{M} , which have vibrational intervals of 520 (17), 530 (20), 526 (16), 533 (15) and 542 (3) cm⁻¹, respectively. Table V lists the band maxima, assignments, and two-photon energies of these progressions. We have assigned these progressions to the ν_2' OPLA modes of five different Rydberg states. As expected for higher Rydberg series members, these REMPI bands appear with much less intensity than those of the \tilde{E} and \tilde{F} Rydberg states. The identification of ν_2 OPLA hot bands ascertains that the \tilde{K} state origin lies at 355.54 nm ($2h\nu = 56\,236$ cm⁻¹) and that the \tilde{L} state origin lies at 354.46 nm ($2h\nu = 56\,409$ cm⁻¹). We assign the origins of the \tilde{J} and \tilde{M} states to lie at the lowest member of each progression at 373.93 nm ($2h\nu = 53\,471$ cm⁻¹) and 346.32 nm ($2h\nu = 57\,733$ cm⁻¹), respectively. Because the \tilde{G} state progression merges with the ν_2 progression of the \tilde{E} state, we will deduce the \tilde{G} origin assignment from a fit of the Rydberg series in the next section.

E. The Rydberg State Assignments and Ionization Potential of the CCl₃ Radical. The Rydberg states observed by this study can be organized into Rydberg series which define the state assignments and the adiabatic ionization potential of the CCl₃ radical. In the absence of strong perturbations the energies of Rydberg state origins conform to the familiar equation:

$$\nu_{0-0} \text{ (cm}^{-1}\text{)} = \text{IP}_a - 109\,737 / (n - \delta)^2$$

where ν_{0-0} is the electronic origin, IP_a is the adiabatic ionization potential in cm⁻¹, n is the principal quantum number, and δ is the quantum defect. Quantum defects may vary only within a limited range for each orbital type. For carbon-centered Rydberg orbitals

the quantum defects (δ) of the ns , np , nd , and nf Rydberg states must lie near 1.0, 0.6, 0.1, and 0.0, respectively.²⁹

The close proximity of the \tilde{E} and \tilde{F} states mandates their assignment to two different Rydberg series. Each series which contains the \tilde{E} and \tilde{F} states will have higher members in the set comprised of the \tilde{G} , \tilde{J} , \tilde{K} , \tilde{L} , and \tilde{M} states. Two self-consistent assignment sequences give the solutions. (1) $\text{IP}_a = 7.56$ eV ($n = 3, 4, 5, 6$; $\delta = 0.18$ for the \tilde{E} , \tilde{J} , \tilde{K} , and \tilde{M} states) and (2) $\text{IP}_a = 8.11$ eV ($n = 3, 4$; $\delta = 0.545$ for the \tilde{E} and \tilde{K} states). Based upon our previously established limits of $\text{IP}_a = 7.9-8.3$ eV, we adopt solution 2.

The quantum defect of solution 2, $\delta = 0.545$, indicates that the \tilde{E} and \tilde{K} states are 3p and 4p Rydberg states. The \tilde{F} and \tilde{L} states form the second np Rydberg series with $n = 3, 4$; $\delta = 0.499$. Because the Rydberg equation describes the relationship between the \tilde{L} and \tilde{F} origins, we can resolve between the candidate bands for the \tilde{F} state origin. We assign the \tilde{F} origin to lie within the congested band at 417.7 nm ($2h\nu = 47\,868$ cm⁻¹).

In the D_{3h} point group the np Rydberg states are divided into states of E' and A_2'' symmetries. Because each np E' symmetry state should lie at lower energy than the corresponding np A_2'' state, we assign the \tilde{E} , \tilde{K} Rydberg series to have $^2E'$ symmetry and the \tilde{F} , \tilde{L} Rydberg series to have $^2A_2''$ symmetry. These symmetry assignments also account for the doublet bands observed in the spectrum of the \tilde{E}^2E' (3p) state. The 33 (5)-cm⁻¹ splitting of each vibrational band arises from spin-orbit interactions.³⁰

(29) Manson, S. T. *Phys. Rev.* **1969**, *182*, 97.

(30) In this text we have labeled the symmetries of the \tilde{E} state using the conventional symmetry notation which ignores the strong coupling between the electron spin and orbital angular momentum. When the spin-symmetries are explicitly incorporated into the overall state symmetry notation, the states we label as $^2E_a'$ and $^2E_b'$ would be called $^2E_{3/2}$ and $^2E_{5/2}$ states. See: Herzberg, G. *Molecular Spectra and Molecular Structure*; Van Nostrand Reinhold: 1966; Vol. 3 pp 14-17.

Table VI. ω_2'' Vibrational Energy Levels Observed for the \tilde{X}^2A_1 Ground State of the CCl₃ Radical and Calculated Using a Quartic Potential, $V = A(Z^4 - BZ^2)$

quantum no. ν_2''	obsd ω_2'' vib energy (cm ⁻¹)	calc ω_2'' vib energy ^a (cm ⁻¹)	difference (obs - calc) (cm ⁻¹)
0	0	0	
1		1.6	
2	251	252	-1
3	290	299	-9
4	466	460	6
5		611	
6		793	

^a $V(\text{cm}^{-1}) = 48.35(Z^4 - 6.16Z^2)$; ZPE = 160 cm⁻¹ for ν_2'' .

In Table V our assignment of the \tilde{J} progression as the 4s Rydberg state, \tilde{J}^2A_1' (4s), is supported by the quantum defect of this state, $\delta = 0.967$. The Rydberg formula solution for the \tilde{M} state origin ($n = 4$, $\delta = 0.217$) supports its assignment as a 4d Rydberg state. This assignment also indicates that the \tilde{G} state is the 3d member of this Rydberg series. The relationship established by the Rydberg formula between the \tilde{M} and \tilde{G} states fixes the \tilde{G} (3d) state origin at 386.40 nm ($2h\nu = 51\,218\text{ cm}^{-1}$) under the $\tilde{E}^2E_a' 2_0^8$ band. The \tilde{G} (3d) 2_1^1 band overlaps with the $\tilde{E}^2E_a' 2_1^9$ band. Under the D_{3h} point group the nd Rydberg series divide into A_1' ($m_l = 0$), E'' ($m_l = \pm 1$), and E' ($m_l = \pm 2$) symmetry states with energies proportional to $-(m_l)$ where m_l is the projection of the orbital angular momentum upon the molecular z axis.³¹ Because the quantum defect of the \tilde{G} , \tilde{M} Rydberg series lies near the maximum expected for the nd Rydberg class, we have tentatively assigned the \tilde{G} , \tilde{M} states to be of $^2E'$ symmetry.

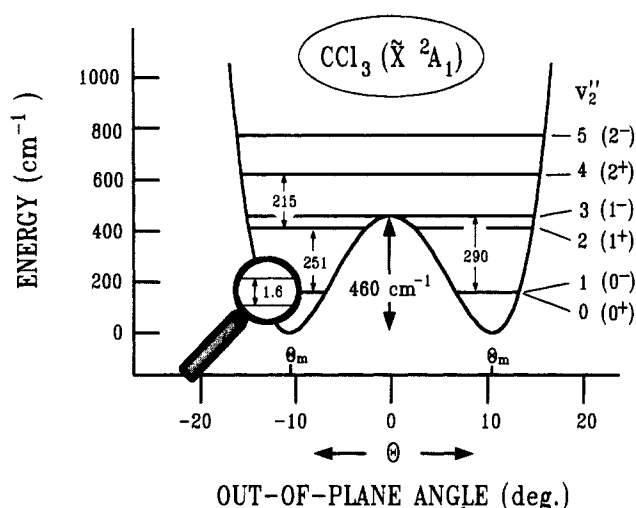
In summary, our assignment scheme fits the observations. As required, each of the three Rydberg series reproduces the IP_a. The combined fit of all three Rydberg series gives IP_a = 65 400(36) cm⁻¹ (8.109 (5) eV).

F. Analysis of the ν_2'' Hot Bands. The \tilde{F}^2E' (3p) $\leftarrow \tilde{X}^2A_1$ REMPI spectrum shows hot bands which reveal the $\nu_2'' = 0-4$ levels of the ground state (Tables III and IV). Table VI lists these ν_2'' OPLA vibrational energy levels. To model the observed energy levels of this double-well potential, we solved the Hamiltonian for the quartic oscillator as described above. Table VI lists the calculated ν_2'' OPLA mode energy levels of the CCl₃ radical obtained with the quartic potential. Using a least-squares procedure, the observed vibrational energy levels were fitted to find the coefficients, listed in the footnote of Table VI. To interpret the equilibrium coordinate value, Z_m , we have adopted the ab initio C-Cl bond length, $r_e = 1.7142\text{ \AA}$ (Table II). The inversion barrier and equilibrium angle derived from these coefficients are $B_{\text{inv}} = 460(40)\text{ cm}^{-1}$ and $\theta_m = 10.6(3)^\circ$ ($\angle\text{Cl-C-Cl} = 116.7(2)^\circ$). Since the residuals listed in Table VI are smaller than the measurement uncertainty of the vibrational intervals (Table IV), the fit is excellent.

Figure 5 diagrams the ν_2'' (a_2'') OPLA mode potential function. The experimentally observed intervals between vibrational levels are also shown. As is typical of vibrations described by double-minimum potentials, the $\nu_2'' = 0-1$ vibrational levels form a nearly degenerate pair separated by 1.6 cm⁻¹. The $\nu_2'' = 2-3$ levels that lie near the crest of the inversion barrier are separated 39 cm⁻¹ apart. Vibrational levels which lie above the inversion barrier are well-separated.

V. Discussion

A. The Electronic States of the CCl₃ Radical. We have assigned the REMPI spectrum of the CCl₃ radical to originate from seven Rydberg states that lie between 47 000 and 58 000 cm⁻¹. The ion signals which produced the spectrum were generated by a 2 + 1 REMPI mechanism. Table VII summarizes the electronic and vibrational frequencies observed for each Rydberg state. In ad-

**Figure 5.** Schematic of the potential function for the ν_2'' (a_2'') OPLA mode of the CCl₃ radical as a function of symmetric out-of-plane bending angle, θ .²⁷ The equilibrium angle at $\theta_m = \pm 10.6^\circ$ corresponds to $\angle(\text{Cl-C-Cl}) = 116.7^\circ$. All energies are in cm⁻¹.**Table VII.** Summary of the Spectroscopic Constants Derived for the Rydberg States Observed in the 2 + 1 REMPI Spectrum of the ¹²C³⁵Cl₃ Radical

Rydberg state	T_0 (cm ⁻¹)	quantum defect ^a	ω_1' (cm ⁻¹)	ω_2' (cm ⁻¹)	spin-orbit splitting (cm ⁻¹)
\tilde{E}^2E' (3p)	47 170	0.547	544 (6)	509 (21)	33 (5)
\tilde{F}^2A_2'' (3p)	47 868	0.498		528 (3)	
\tilde{G}^2E' (3d) ^b	51 218	0.218		520 (17)	
\tilde{J}^2A_1' (4s)	53 471	0.967		530 (20)	
\tilde{K}^2E' (4p)	56 236	0.540		526 (16)	
\tilde{L}^2A_2'' (4p)	56 409	0.506		533 (15)	
\tilde{M}^2E' (4d) ^b	57 733	0.217		542 (3)	

^a Based upon IP_a = 8.109 eV. ^b Tentative symmetry assignment. See the text.

dition, the assignment of ν_2'' vibrational hot bands enabled a determination of the ground-state ν_2'' OPLA potential.

The present two-photon REMPI spectrum of the CCl₃ radical overlaps in energy with the one-photon absorption spectrum observed between 38 400 and 51 300 cm⁻¹ by others. Lesigne et al.⁸ have reported a strong UV absorption spectrum of CCl₃ radical in the liquid phase. More recently, Danis et al.⁹ and Russell et al.¹⁰ have measured the same absorption spectrum between 195 and 260 nm in the gas phase. The gas-phase spectrum consists of an intense, unstructured band which displays a maximum at $211 \pm 2\text{ nm}$ and an absorption tail which extends to 260 nm. This spectrum suggests that the origin of this 211-nm band lies near 40 000 cm⁻¹.

The candidate assignments for the 211-nm band are the \tilde{D}^2E valence state and the \tilde{C}^2A_1' (3s) Rydberg state. The Rydberg formula predicts that the \tilde{C}^2A_1' (3s) Rydberg state should lie near 38 800 cm⁻¹. We estimate that the \tilde{D}^2E valence state origin should lie somewhat below 44 000 cm⁻¹ (see section II). The data presented in the literature are insufficient to resolve between these assignments. In the region of energy overlap between the REMPI and UV data our REMPI spectrum shows no bands that we can assign to this band system. The continuous band contour of the 211-nm band suggests that the upper state may suffer from predissociation or rapid nonradiative decay. Either process could quench REMPI signal generation.¹⁶

B. Comparison of ab Initio Calculations and Experimental Results. The ab initio structures calculated for the CCl₃ radical and cation (Table II) conform to the predictions we derived from the QMOT descriptions. The cation is planar and the radical is pyramidal. The ab initio results show that the C-Cl bond length in the cation is shorter than in the radical. The QMOT description predicts that the longer bond length in the radical arises from the out-of-phase repulsions between the carbon and chlorine p_z AO's

(31) Hudgens, J. W.; DiGiuseppe, T. G.; Lin, M. C. *J. Chem. Phys.* **1983**, *79*, 571.

in the SOMO, π^* -MO 29 (Figure 1). However, the slight lengthening of the C-Cl bond as CCl_3 transforms from the D_{3h} to the C_{3v} equilibrium structure (Table II) is due to higher order effects not easily seen from the QMOT description.

This paper is the first to report ab initio calculations of the CCl_3 cation. Table II presents the ab initio structure and scaled vibrational frequencies. Only the ν_3 degenerate stretch frequency of the cation is experimentally known. The scaled ab initio ν_3 frequency computed at the HF/6-31G* level agrees closely with the observed frequency. To enable a more complete comparison of the cation vibrational frequencies listed in Table II, we have adopted the ν_1 and ν_2 vibrational frequencies of the \tilde{E}^2E' (3p) CCl_3 Rydberg radical as surrogates for those of the cation. Because the molecular bonding in the core of CCl_3 Rydberg radicals closely resembles the bonding in the cation (section II), these substitutions are reasonable. The scaled ab initio ν_1 and ν_2 frequencies differ from the \tilde{E}^2E' (3p) Rydberg radical frequencies by 4% and 2%, respectively.

From our experimental data we have derived the \tilde{X}^2A_1 CCl_3 radical apex angle, $\angle(\text{Cl}-\text{C}-\text{Cl}) = 116.7 (2)^\circ$ ($\Theta_m = 10.6 (3)^\circ$). The experimental angle and the apex angle found by ab initio calculation are in good agreement. At the UHF/6-31G* level Luke et al.³² and Moc et al.³³ have found the same optimized structure reported here, $\angle(\text{Cl}-\text{C}-\text{Cl}) = 117.1^\circ$ ($\Theta_m = 9.9^\circ$) and $r_e(\text{C}-\text{Cl}) = 1.7142 \text{ \AA}$. In an earlier work performed at the UHF/4-31G level of theory, Moc et al.³⁴ found $\angle(\text{Cl}-\text{C}-\text{Cl}) = 116.5^\circ$ ($\Theta_m = 10.9^\circ$) and $r_e(\text{C}-\text{Cl}) = 1.776 \text{ \AA}$. The main difference between the UHF/6-31G* and UHF/4-31G optimized structures appears in the computed C-Cl bond lengths. The longer bond length obtained with the UHF/4-31G level of theory originates from the absence of polarization functions in the 4-31G basis set.³⁴

Table II also presents the scaled vibrational frequencies of the \tilde{X}^2A_1 radical derived from the UHF/6-31G* ab initio calculations. (Russell et al.¹⁰ also report similar scaled UHF/6-31G* ab initio frequencies except that they treat the ν_2 mode as a harmonic oscillator.) The close agreement between the ν_3 degenerate stretch frequencies found by the scaled ab initio calculations and by experiment is encouraging and suggests that the other harmonic modes, ν_1 and ν_4 , should also agree with these calculations. In contrast the $\nu_2'' = 2-0$ OPLA frequency interval predicted from the optimized UHF/6-31G* ab initio calculation differs significantly from the experimental interval (Table II).

The ν_2 OPLA vibrational energy manifold is sensitive to the equilibrium structure and the inversion barrier. In this work the larger disagreement between experiment and theory resides with the magnitude of the inversion barrier, B_{inv} . The least-squares fit of the spectral data gives $B_{\text{inv}} = 460 (40) \text{ cm}^{-1}$. Our ab initio barriers (Table I) calculated at several levels of theory all lie 150–385 cm^{-1} higher than the experimentally derived barrier. Ab initio calculations by others are also greater than the experimental B_{inv} . At the UHF/6-31G* level Luke et al.³² and Moc et al.³³ find the same inversion barrier as reported here, $B_{\text{inv}} = 610 \text{ cm}^{-1}$. Moc et al.³³ have studied the effect of basis sets on B_{inv} in the CCl_3

radical. They have found that when the CCl_3 geometry is optimized and B_{inv} is calculated using the same basis set, B_{inv} will decrease as the size of the basis set is increased. But when the CCl_3 geometry is optimized with one basis set and then B_{inv} is calculated by a single point calculation which uses an expanded basis set, B_{inv} increases.

Our previous experience with the CHCl_2 radical leads us to believe that lower B_{inv} 's will be obtained by using structures optimized at a theory levels that include electron correlation. During our study of the CHCl_2 radical²¹ the single-point UMP4 = FC/6-31G* calculation that used the radical and transition structure geometries optimized at the UMP2/6-31G* level yielded a B_{inv} which was 25% lower than the single-point calculation that used geometries optimized only at the UHF/6-31G* level. If a similar reduction in B_{inv} were to occur for the CCl_3 radical by using the radical and transition structure geometries found at the UMP2/6-31G* level of theory, then the ab initio and experimentally derived B_{inv} 's would agree within 10%. Unfortunately, for this study computer memory limitations thwarted our attempts to optimize the CCl_3 radical geometry at the UMP2/6-31G* level of theory.

Table I shows the adiabatic ionization potentials of CCl_3 radical computed at several levels of theory. At the UHF/6-31G* level of theory these calculations give $\text{IP}_a = 8.25 \text{ eV}$ which is only $\sim 0.1 \text{ eV}$ higher than the experimental IP_a (Table II). But single-point calculations at higher levels of theory which use these UHF/6-31G* structures underestimate the IP_a by 0.26–0.59 eV. We interpret the failure of the present ab initio calculations to reproduce the observed IP_a as additional evidence that the optimized CCl_3 radical geometry will continue to change significantly as electron correlation corrections are added to the calculations.

The ab initio calculation of IP_a is a differential measurement on the convergence of the optimized geometries for the cation and radical. Because the cation is a closed-shell configuration with fewer electrons than the radical, its ab initio geometry will converge more rapidly to the true geometry than will the radical structure. Thus, the CCl_3 cation structure found at the HF/6-31G* level of theory should be more accurate than the CCl_3 radical geometry found at the UHF/6-31G* level. For the CCl_3 cation single point calculations at higher levels of theory should almost give the maximum total energy reduction. But if the UHF/6-31G* level of theory cannot find a sufficiently accurate geometry for the CCl_3 radical, then single point calculations at higher theory levels will not give the maximum energy reduction. Thus, the IP_a 's derived from single point calculations at higher levels of theory should underestimate IP_a , as observed. We conclude that accurate ab initio calculation of IP_a will require the computation of an optimized CCl_3 radical geometry at the UMP2/6-31G* level, or higher.

Acknowledgment. Dr. Sherif A. Kafafi acknowledges the financial support of the A. Mellon Foundation and the Johns Hopkins University School of Public Health Academic Data Center for the allocated computer time. Dr. Bilin P. Tsai thanks the University of Minnesota for support through the Bush Sabbatical Program. We wish to thank Dr. David Gutman (Catholic University of America, Washington, DC) and Dr. Wing Tsang (NIST, Gaithersburg, MD) for useful discussions. We thank Dr. Jerzy Moc (University of Wroclaw, Wroclaw, Poland) for sending us a preprint of their results.

(32) Luke, B. T.; Loew, G. H.; McLean, A. D. *J. Am. Chem. Soc.* **1987**, *109*, 1307.

(33) Moc, J.; Rudzinski, J. M.; Latajka, Z.; Ratajczak, H. *Chem. Phys. Lett.* **1990**, *168*, 79.

(34) Moc, J.; Latajka, Z.; Ratajczak, H. *Z. Phys. D* **1986**, *4*, 185.